Hindawi
Journal of Nanotechnology
Volume 2024, Article ID 6687926, 15 pages
https://doi.org/10.1155/2024/6687926

Research Article

Synthesis, Characterization, and Photocatalytic Performance of $ZnFe_2O_4$-g-C_3N_4 Composites for Tetracycline Removal from Contaminated Water

Humphrey Mutuma Samuel,[1,2] **Milton M. M'Arimi**,[1] **and Cleophas Achisa Mecha**[1,2]

[1]*Department of Chemical and Process Engineering, Moi University, P.O. BOX 3900-30100, Eldoret, Kenya*
[2]*Renewable Energy, Nanomaterials and Water Research Group, Moi University, P.O. BOX 3900-30100, Eldoret, Kenya*

Correspondence should be addressed to Cleophas Achisa Mecha; achisacm@mu.ac.ke

Received 6 July 2023; Revised 9 February 2024; Accepted 8 March 2024; Published 18 March 2024

Academic Editor: Marco Rossi

The presence of emerging contaminants in wastewater like tetracycline poses a significant challenge in water reuse worldwide. The implementation of a p-n heterojunction and dye-sensitized techniques in the enhancement of graphite carbon nitride provides a promising alternative for visible light-driven degradation of emerging contaminants present in wastewater. The present study investigated dye-sensitized and plain composites in degrading tetracycline using natural sunlight in a parabolic trough reactor. The study synthesized four composites of $ZnFe_2O_4$-g-C_3N_4 at 5, 15, and 25 wt% loading of the ferrite by direct annealing of melamine, followed by thermal and ultrasonic exfoliation of bulk graphite carbon nitride and in situ precipitation with zinc ferrites to yield a composite photocatalyst. The photocatalysts were characterized using X-ray diffraction (XRD) analyses which confirmed that all the spinel ferrite phases of $ZnFe_2O_4$ were well bonded with g-C_3N_4 nanosheets to form a composite. The crystallite sizes were calculated by the Debye–Scherrer equation indicating crystal sizes of between 4.63 and 8.61 nm confirming the nanostructures. The scanning electron microscope-energy dispersive spectroscopy (SEM-EDX) tests verified that the spherical globules of $ZnFe_2O_4$ were well attached to the mesoporous layers of g-C_3N_4 and absence of contaminant phases. The UV-Vis analysis for 25% ZF-GCN revealed a band gap reduction from 2.67 eV to 2.03 eV. The PL intensity for all the composites decreased at excitation of 266 nm and 550 nm which was evidence for suppressed charge recombination. A 25% ferrite loading resulted in the best photocatalytic performance with tetracycline degradation of 93.64% and total organic carbon (TOC) removal of 51.89%. The sensitization of the 25% ZF-GCN composite with Eosin Y further improved its performance for degradation of tetracycline to 94.62% and TOC removal to 68.29%. Therefore, dye sensitization is an efficient way of improving the photocatalytic activity of a multicomponent photocatalyst for the removal of emerging pollutants.

1. Introduction

The rising standards of living witnessed in many developing countries have been accompanied by rapid industrialization, urbanization, and population growth. This has consequently contributed to the uncontrolled release of emerging pollutants to aquatic bodies and thus led to a severe strain on existing freshwater sources [1]. These emerging pollutants can be broadly classified into organic compounds (pharmaceuticals, personal care products, pesticides, polyaromatic compounds, and dyes), inorganic compounds (heavy metals, fertilizers, and radioactive compounds), and pathogens, which can potentially cause devastating effects in the ecosystem [2].

Pharmaceuticals and personal care products are the most commonly detected emerging pollutants in water bodies [3]. Some of these contaminants have stable structures, are highly carcinogenic, and are poorly removed by conventional wastewater treatment facilities, which consequently results in their disposal in freshwater bodies [4, 5]. The existing conventional wastewater treatment techniques rely majorly on physical, chemical, and biological methods [6].

These plants are designed to remove nutrients and biodegradable organics at high efficiencies and low costs. However, emerging pollutants such as antibiotics can be toxic to the bacteria which results in poor degradation and mineralization commonly associated with these conventional plants [7]. One such notorious emerging contaminant is tetracycline, a multipurpose antibiotic extensively applied for treating infections caused by both Gram-negative and Gram-positive bacteria in both humans and animals [8]. This antibiotic can only be partially metabolized in humans, is chemically stable in water matrices, and has antibacterial properties which hinder its elimination by biological/chemical systems [9, 10]. Furthermore, it is the second most manufactured antibiotic in the world, hence a higher likelihood of its residues accumulating in aquatic systems [11]. These residues may induce the proliferation of antibiotic-resistant bacteria and genes, which could be more harmful than antibiotics thus causing ecological problems [12, 13]. Therefore, there is an urgent need to eliminate its residues from water bodies.

Advanced oxidation processes (AOPs) are increasingly explored as alternatives to conventional treatment plants for eliminating emerging pollutants. Among AOPs, heterogenous photocatalysis has gained prominence due to its suitable properties, such as the ability to use solar energy, high pollutant removal efficiency, recyclable photocatalyst, highly nonselective process, and mild condition operations. Furthermore, it does not generate secondary pollutants and is environmentally friendly [14, 15]. This process involves photoexcitation of a semiconductor using light photons that are more energetic than the band gap. The process photogenerates electrons and holes, which form superoxide and hydroxide oxidative radicals that can degrade pollutants [2]. Some of the potential applications for heterogenous photocatalysis include (i) pretreatment of high industrial strength organic wastes to enhance their biodegradability before biological treatment, (ii) posttreatment or polishing step for emerging pollutant removal at low concentrations, and (iii) disinfection of potable water [1].

Recently, graphite carbon nitride (g-C_3N_4) has gained attention as a promising heterogenous photocatalyst. It is a metal-free, n-type semiconductor with a π-conjugated polymeric structure and has abundant delocalized electrons [16]. Additionally, its band gap energy of (~2.7 eV) is capable of utilizing visible light up to 460 nm and has well-positioned valence and conduction bands which are appropriate for water oxidation. Therefore, due to its rare optoelectronic, structural, and chemical properties, it has been widely tested as an ideal semiconductor in water splitting, pollutant degradation, and energy storage field [17, 18]. However, g-C_3N_4 suffers from a plethora of pitfalls, such as a small interstitial surface area, rapid recombination of photogenerated charges, and low quantum yields due to poor electron mobility which hinders its photocatalytic performance [16, 19, 20]. To improve the photocatalytic performance of g-C_3N_4, various techniques can be employed, such as exfoliation, construction of heterojunctions, and dye sensitization [11, 21].

The issue of a small surface area can be addressed by the application of exfoliation techniques, which can separate the bulk g-C_3N_4 into 2-D structures by breaking weak van der Waals forces between the layers. This results in nanosheets that have a high specific surface area, hence increased reaction sites, lower recombination rates of electrons/holes due to reduced diffusion paths, and thus better electronic properties [17]. Nevertheless, single photocatalytic systems have inadequate photocatalytic performance and are often inferior to multicomponent photocatalysts [20]. Therefore, there is an increasing trend to combine multiple photocatalysts to form composites. These composite semiconductors form heterojunctions that create an internal electric field necessary for driving opposite charges in the two semiconductors. This enhances charge separation and thus decreases charge recombination [22, 23]. Several studies have worked to improve on the photocatalytic performance of g-C_3N_4 by combining it with $ZnFe_2O_4$ to form a composite. Borthakul and Saikia synthesized a composite of 10% $ZnFe_2O_4$/g-C_3N_4 using the coprecipitation method and achieved 97.4% of rhodamine B removal in 30 minutes using visible light [24]. Similarly, Renukadevi and Jeyakumari synthesized 15% $ZnFe_2O_4$/g-C_3N_4 using the microwave irradiation method and achieved 86% and 98% removal of methyl orange and rhodamine B dye, respectively, in 60 minutesThese studies are evidence that the photocatalytic activity of g-C_3N_4 is improved by creating a composite with $ZnFe_2O_4$. Furthermore, $ZnFe_2O_4$ belongs to the spinel-ferrite family whose compounds have extensive visible light absorption up to $\lambda < 653$ nm and have better charge mobility and ferromagnetic properties, which can enable magnetic separation at the end of treatment [26].

Nevertheless, most previous studies have worked on exfoliation techniques and creating composites as the main modification for g-C_3N_4. This research has attempted to study the effect of dye sensitization on the best-performing $ZnFe_2O_4$/g-C_3N_4 composites. Dye sensitization is a promising approach since dye molecules can be excited at long wavelengths by visible light photons to produce electrons from its HOMO band (highest occupied molecular orbital), which is passed to its LUMO band (lowest unoccupied molecular orbital) and subsequently injected to the conduction band of the semiconductor [27, 28]. These injected electrons then react with adsorbed oxygen molecules on the surface of the photocatalyst to form superoxide, hydroxyl, and other active species [29]. Eosin Y is an anthracene-based dye with a high optical absorption coefficient necessary for the absorption of visible light at long light wavelengths [30]. Furthermore, due to its low cost, it can be used as a potential sensitizer.

Considering the surging energy cost, utilizing solar energy to drive heterogenous photocatalytic systems has become a priority for researchers. The parabolic trough reactor (PTR) is a promising configuration for wastewater remediation adopted from thermal power concentrators [31]. It has a parabolic shape that reflects solar rays along a focal line where a collector tube holding wastewater is positioned [32]. A tracking system is installed in order to maintain the incident solar rays perpendicular to the

receiver at various sun positions. The PTR can be utilized in photochemical reactions, due to its ability to concentrate high-energy photons for photocatalyst activation [33]. Besides, it can be operated at high fluid throughput, which is necessary to maintain turbulent flow regimes. This consequently promotes turbulent diffusion which enhances mass transfer between contaminant and photocatalyst surface [34, 35]. However, the PTR is flawed since it only concentrates direct sunlight but not the diffuse radiation. Hence, it is applicable to summer conditions [36].

Nevertheless, some studies have reported solar-assisted heterogenous systems to outperform both UV and visible light. Ghaedi et al. compared the performance of two cationic dyes (rhodamine B and methylene blue) under solar light (PTR) and visible light (LED) using a g-C_3N_4/TiO_2 composite [37]. The study showed that solar light had faster degradation kinetics than LED light. The apparent kinetic constants for solar light were 1.29 and 1.18 times faster than LED for methylene blue and rhodamine B, respectively. Rani et al. investigated the degradation of doxycycline (DOX) and ofloxacin under solar, UV, and visible light using a TiO_2-SiO_2-Fe photocatalyst [38]. The highest photocatalytic performance was achieved under solar light as compared to UV and visible light. The degradation efficiency for ofloxacin after 15 min was 24%, 45.6%, and 98.16% for visible, UV, and solar light, respectively. Therefore, considering these desirable capabilities, the PTR is a promising solar reactor that was utilized in this study.

The present study aims to examine the effect of dye sensitization in the photocatalytic performance of a composite by synthesizing Eosin Y-sensitized $ZnFe_2O_4$/g-C_3N_4 composite. To the best of our knowledge, several reports have been published on the degradation of organic dyes with $ZnFe_2O_4$/g-C_3N_4 composite. Nonetheless, no study has been reported of Eosin Y-dye-sensitized $ZnFe_2O_4$/g-C_3N_4 composite for tetracycline degradation. Furthermore, only a few studies have used natural solar light. Hence, for greater practicability of heterogenous photocatalysis, this study investigated the performance of photocatalysts under solar light using a solar parabolic trough reactor. Thus, the current study (i) synthesized Eosin Y sensitized and plain $ZnFe_2O_4$/g-C_3N_4 composite at weight ratios of 5, 15, and 25%, (ii) characterized the structural, morphological, chemical composition, and photoelectronic properties of composites using XRD, FTIR, SEM-EDX, UV-Vis, and PL spectra, and (iii) evaluated the photocatalytic performance of composites and pure semiconductors in the degradation of tetracycline.

2. Materials and Methods

2.1. Materials. All reagents used in this study were of analytical grade and used without any further purification. Melamine powder (Sigma-Aldrich), deionized water, dilute ammonia solution, iron (III) chloride hexahydrate (Sigma-Aldrich), zinc (II) chloride dehydrate (RD HAEN), Eosin Y-dye (Kobian Chemicals), ethanol, hydrogen peroxide (Kobian chemicals), tetracycline (Universal Corporation), 0.2 M HCl (Kobian chemicals), and 0.2 M NaOH (Kobian chemicals).

2.2. Synthesis of Photocatalyst

2.2.1. Preparation of g-C_3N_4. Graphite carbon nitride (g-C_3N_4) was synthesized using methods adapted from [39–41] with modification implemented being thermal and ultrasonic exfoliation of bulk graphite carbon nitride to obtain nanosheets. In a typical experiment, 20 grams of melamine powder was placed in a closed alumina crucible and the crucible was then heated at 550°C at a heating rate of 5°C/minute for 4 hours in a furnace (Carbolite Gero Furnace, ELF 11/14). The resultant product was then finely ground into powder and then heated to 550°C for 2 hours in open air to obtain g-C_3N_4 nanosheets. The graphite carbon nitride formed was then ultrasonically dispersed in 200 ml of water for 15 hours. The resultant suspension was then centrifuged at 150 rpm to aid in the separation of any unexfoliated graphite carbon nitride. The supernatant solution was then oven-dried (Daihan Labtech, LDO-150) at 70°C for 24 hours to obtain pure graphite carbon nitride. The obtained graphite carbon nitride was then ground into fine powder.

2.2.2. Preparation of $ZnFe_2O_4$/g-C_3N_4. The preparation of $ZnFe_2O_4$/g-C_3N_4 photocatalyst followed a coprecipitation procedure with the method adapted from [25, 40, 41]. In a typical experiment, 20 grams of graphite carbon nitride were ultrasonically dispersed for 30 minutes in 100 ml of water. Iron (III) chloride hexahydrate (0.0124 M) and zinc (II) chloride dehydrate (0.0248 M) were then added to the graphite carbon nitride and then stirred using a magnetic stirrer (Pro Scientific) for one hour. After the metal salts dissolved completely, the reaction mixture was then heated at 80°C and ammonium hydroxide was added dropwise periodically to adjust pH to 10 to aid in precipitation. The mixture was then stirred for another 4 hours and then allowed to precipitate. The generated precipitate was then washed first with deionized water, followed by ethanol three times, and then dried at 80°C overnight in a vacuum oven. Finally, the synthesized composite was annealed at 500°C for 2 hours to improve the crystal structure. Other hybrids of $ZnFe_2O_4$-g-C_3N_4 were synthesized using the same procedure at different weight ratios of 5, 15, and 25%.

2.2.3. Dye Sensitization of $ZnFe_2O_4$/g-C_3N_4. The dye sensitization experiment used mixing and adsorption with the method adapted from [28, 42]. In a typical experiment, 10 grams of photocatalyst was added to 100 ml of ethanol solution and stirred magnetically for thirty minutes to ensure even mixing. Half a gram of Eosin Y dye was then added to the slurry and then stirred for 24 hours. The resultant solid residue was subsequently rinsed thrice with deionized water, followed by 99% ethanol. The washed solid precipitate was oven-dried at 80°C for 8 hours to obtain a dye-sensitized photocatalyst, which was then stored in amber bottles. Figure 1 summarizes the process route used in synthesizing the photocatalysts.

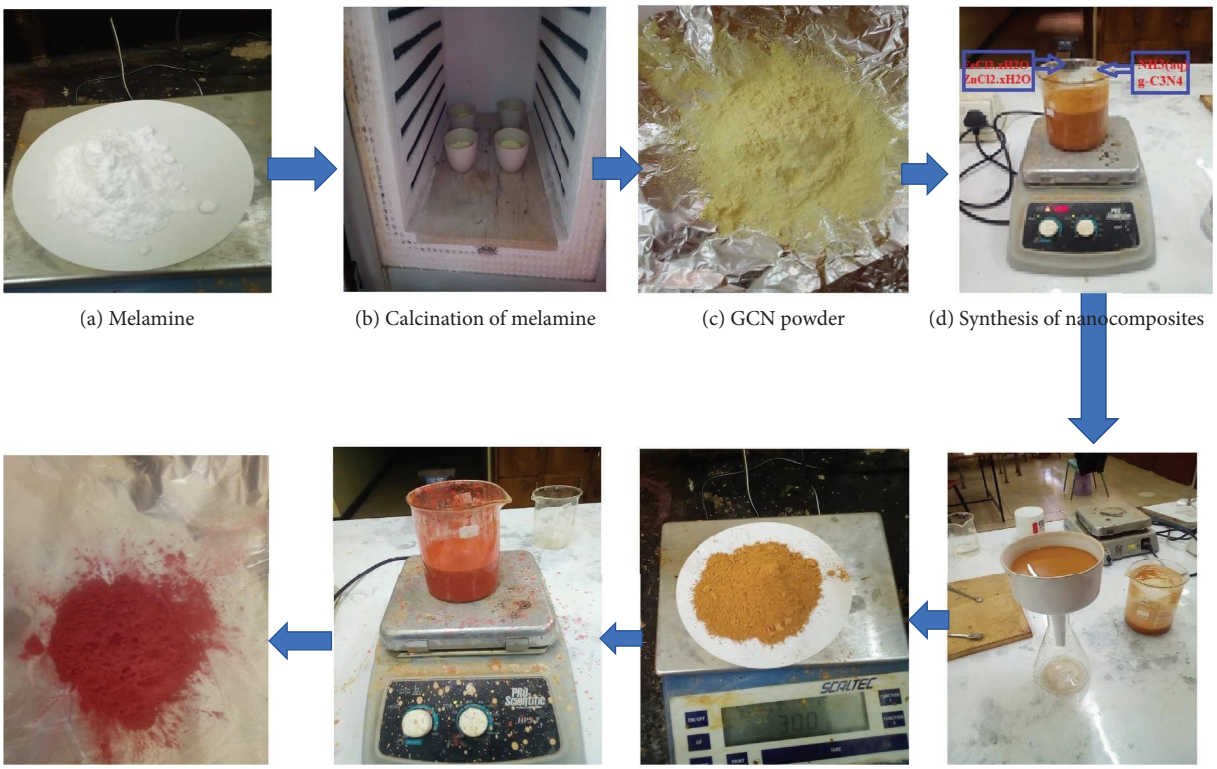

(a) Melamine (b) Calcination of melamine (c) GCN powder (d) Synthesis of nanocomposites

(h) Dried sensitized composite (g) Dye sensitization of composite (f) Dried nanocomposites (e) Filtration of precipitate

Figure 1: A summarized process route used in synthesizing photocatalyst (5, 15, and 25% $ZnFe_2O_4$/g-C_3N_4 and EY-25%-$ZnFe_2O_4$/g-C_3N_4).

2.3. Characterization of Photocatalysts

2.3.1. XRD. The crystalline structure and patterns of the photocatalysts were analyzed using a Rigaku Altima III X-ray diffractometer equipped with Cu Kα radiation ($\lambda = 1.54178$ Å) at a scanning angle of 10–90°. The average crystallite sizes of the five composites were calculated using the Debye–Scherrer equation [43].

$$D = \frac{K\lambda}{\beta \cos \theta}, \tag{1}$$

where D = crystallite size, K = shape factor of sphere taken as 0.9, β = full width at half maximum (FWHM) radians, λ = X-ray wavelength (0.154178 nm), and θ = Braggs angle.

2.3.2. FTIR. The functional groups and their vibration modes were determined using a Fourier transform infrared spectrometer (FT-IR, PerkinElmer Frontier) for the range 4000–500 cm^{-1}.

2.3.3. SEM-EDX. Scanning electron microscopy (SEM) is a technique that involves focusing a strong electron beam on a sample, which causes electrons to interact with the surface to obtain the surface topography and microstructure of a sample. The morphology, microstructure, and the chemical composition of the photocatalyst were determined using a scanning electron microscope equipped with energy dispersive X-ray spectroscopy (SEM-EDS, Zeiss-Ultra 55) operating at 3 KV.

2.3.4. UV-Vis. The optical absorption properties of the photocatalyst were determined using a UV-Vis absorption spectrophotometer (Shimadzu, UV-1800) for the range 200–800 nm. A small sample of the photocatalyst was first ultrasonically suspended using distilled water in a 100 ml beaker. This was then followed by a UV-Vis wavelength scan in the 200–800 nm wavelength. A tangent line was drawn from the descending absorption spectrum to obtain the tail absorption edge, which can be used to calculate the band gap energy according to equation (2) [43, 44]:

$$E_g = \frac{1240\text{eV}}{\lambda_{\max}}. \tag{2}$$

2.3.5. PL-Spectra. The photoelectronic properties of the photocatalysts were determined using a photoluminescence spectrum (PL, Horiba LabRam HR) at an excitation wavelength of 266 and 550 nm.

2.4. Photocatalytic Performance. The photocatalytic performance of various as-prepared photocatalysts was tested by solar photodegradation of tetracycline in a slurry parabolic trough reactor (PTR), and the equipment setup is shown in Figure S1 in the supplementary material. The experiment was conducted between the sunny months of January-March 2023, in Eldoret, Kenya, at a solar irradiance of between 900 and 1050 W/m^2. For a typical experiment, 0.7 g of photocatalyst was mixed with 10 mg/l of tetracycline dissolved in

1.5 L of distilled water. The resultant mixture was then magnetically stirred for 15 minutes in a dark room to establish the adsorption-desorption equilibrium. The solution was then irradiated using a PTR. A 5 ml sample was then drawn at periodic intervals of 0, 30, 60, and 90 minutes. The sample was then centrifuged and filtered using a 0.45 μm syringe filter. The sample was then measured at 358 nm (max absorbance for tetracycline) using a UV-Vis spectrophotometer (UV-1800, Shimadzu). The concentration of tetracycline was then determined from the UV absorbance curves calibrated based on De Beers' law. The collected samples were also analyzed for total organic carbon using a TOC analyzer (Multi N/C 2100, Analytica Jena) to confirm the degree of mineralization. The tetracycline degradation efficiency was calculated according to the following equation:

$$\text{Degradation Efficiency}\,(\%) = \frac{C_o - C_t}{C_o} * 100. \quad (3)$$

The degradation kinetics were analyzed using the pseudo-second-order equation:

$$\frac{1}{C_t} - \frac{1}{C_o} = k_{\text{app}} t, \quad (4)$$

where C_o = initial concentration, C_t = concentration at time t (mg/l), and k_{app} = apparent kinetic constant ($\text{mg}^{-1}\cdot\text{L}\cdot\text{min}^{-1}$).

The mineralization efficiency was determined by the following equation:

$$\text{TOC removal}\,(\%) = \left(1 - \frac{\text{TOC}_t}{\text{TOC}_o}\right) * 100, \quad (5)$$

where TOC_o = initial TOC concentration and TOC_t = final TOC concentration, mg/l

3. Results and Discussion

3.1. Characterization of the As-Synthesized Photocatalysts

3.1.1. Structural Analyses of Photocatalyst

(1) XRD Analyses. The XRD patterns for pure g-C_3N_4, $ZnFe_2O_4$, and their hybrids were recorded at angle 2θ for the range between 10 and 90°. Figures 2(a) and 2(b) show the diffraction planes of the pure photocatalysts and their composites.

Pure g-C_3N_4 had a characteristic intense peak at 27.5°, and this peak corresponds well to a width of 0.326 nm and represents the crystallographic plane (002) according to (JCPDS98-1526) [45]. This diffraction plane represents the interlayer packing of the graphitic melon network present in g-C_3N_4. Similarly, another smaller peak at 13.1° was observed in g-C_3N_4. This peak was indexed in the crystallographic plane (100) and was as a result of repeated s-triazine units' packing. These results were within the literature values since most studies have found g-C_3N_4 to have two diffraction peaks ranging from 12.8 to 13.41° and 27.2 to 27.8° [24, 40].

Moreover, for $ZnFe_2O_4$, a series of small intense diffraction peaks were observed at 29.9°, 35.2°, 42.8°, 49.4°, 54.1°, 56.5°, and 62.3°. These peaks were well matched with the spinel ferrite structure (JCPDS77-0011) of crystallographic planes of (220), (311), (400), (422), (511), and (440) [41]. Additionally, no impurity phases of Fe_2O_3 were identified in $ZnFe_2O_4$, which was evidence for the successful synthesis of the spinel ferrite structure and high degree of crystallinity. On the other hand, most diffraction peaks attributable to pure $ZnFe_2O_4$ and g-C_3N_4 could be observed in the XRD patterns of the composites as shown in Figure 2(b). However, for the 5% ZF-GCN composite, only the 35.2° $ZnFe_2O_4$ peak could be observed. This agrees with literature since low quantities of $ZnFe_2O_4$ may not be detected by the XRD [46]. Hence, the existence of both phases in the composites was evidence of the successful incorporation of $ZnFe_2O_4$ nanoparticles in the crystalline structure of g-C_3N_4 and thus successful construction of the heterostructure.

Table 1 shows the crystallite sizes of the as-prepared photocatalysts. These results confirmed the formation of nanoparticles since the average crystal size ranged between 4.63 and 8.51 nm. These values were comparable to the average crystallite size results obtained by Saeed et al. for $Mn_{0.6}Zn_{0.4}Fe_2O_4$/g-C_3N_4 photocatalyst which ranged between 5.8 and 6.96 nm [47].

Interestingly, it was observed that by increasing the percentage of $ZnFe_2O_4$ in the composite, there was significant suppression of g-C_3N_4 peaks, while the intensity of $ZnFe_2O_4$ peaks steadily increased [45, 46]. For instance, the 13.2° peak was almost completely diminished in the 25% ZF-GCN composite. Similarly, on close examination of the composite peaks, there was a slight shift to higher diffraction angles, which has also been reported in the literature [48]. Likewise, the g-C_3N_4 peak shifted slightly from 27.5° to 27.6°. These observations could suggest that by creating the heterostructure, there is a remarkable decrease in the overall crystallinity and dispersibility of the composite [25]. Moreover, these occurrences could be explained by the possible guest-host interaction between g-C_3N_4 and the metal ions. Nonetheless, the XRD spectra of Eosin Y-sensitized (25% ZF-GCN) and the unsensitized (25% ZF-GCN) hybrids were almost identical. This could imply that dye sensitization at small concentrations has little effect on the crystalline structure of the composite, and they interact through van der Waals or hydrogen bond as reported for similar studies involving dye sensitization [29].

(2) FTIR Analyses. Pure g-C_3N_4 and its composites showed intense peaks at 808 cm^{-1}, as shown in Figure 3.

This was due to the stretching mode of carbon-nitrogen heterocycles attributed to the breathing mode of the s-triazine rings [49]. Additionally, for g-C_3N_4 and its composites, other characteristic peaks were noticed in the region between 1200 and 1600 cm^{-1} region with specific peaks at 1241, 1325, 1413, 1455, and 1637 cm^{-1}. These series of peaks were attributed to the aromatic stretching vibration of C=N heterocyclic ring as a consequence of heptazine repeating units [50]. Also, another broad absorption peak was observed between 2940 and 3644 cm^{-1}. This could be due to the vibration of NH and NH_2 terminal groups at defect size or the breathing mode due to adsorbed water molecules [10].

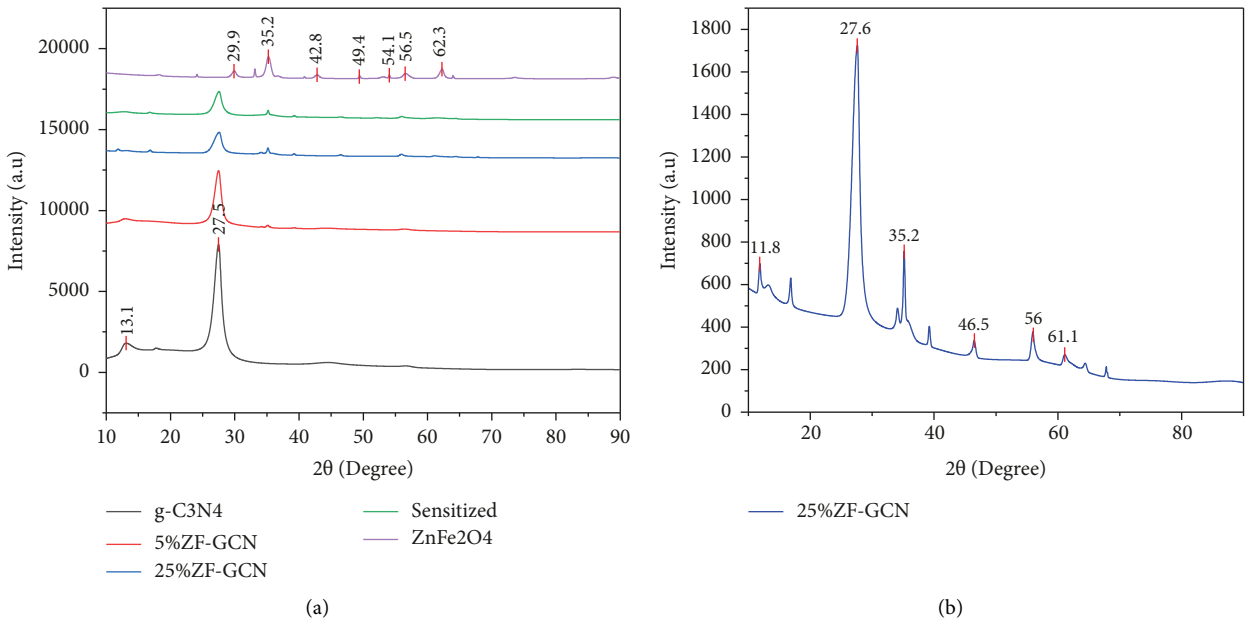

Figure 2: (a) XRD diffraction patterns for g-C_3N_4, $ZnFe_2O_4$ and hybrids (5% ZF-GCN, 25%ZF-GCN, EY-25%ZF-GCN) (b) 25% ZF-GCN showing the diffraction peaks of both photocatalysts.

Table 1: Average crystallite size of photocatalysts.

Photocatalyst	2θ	FWHM	D (nm)
g-C_3N_4	27.48	1.51334	5.103
$ZnFe_2O_4$	35.2	0.89038	8.511
5% ZF-GCN	27.48	1.34715	5.732
25% ZF-GCN	27.6	1.66573	4.635
Sensitized	27.56	1.59701	4.835

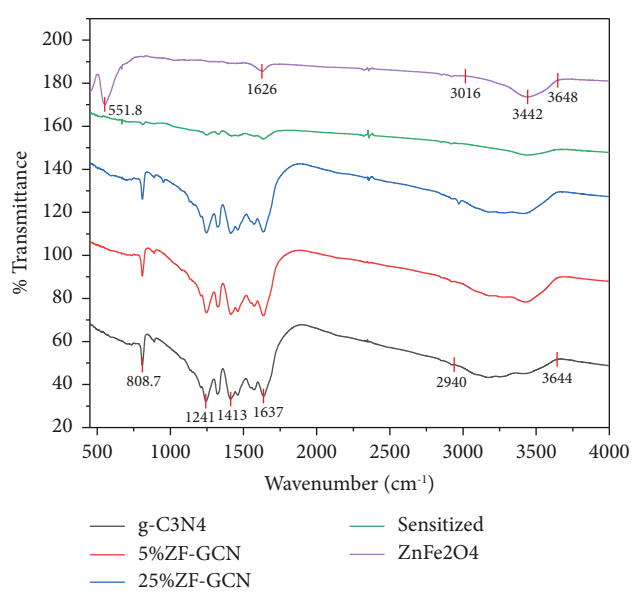

Figure 3: FTIR spectra analyses for g-C_3N_4, $ZnFe_2O_4$ and hybrids (5% ZF-GCN, 25% ZF-GCN, sensitized 25% ZF-GCN).

On the other hand, for $ZnFe_2O_4$, characteristic intense peaks were identified at 3442 cm^{-1} and 1626 cm^{-1}. These could be attributed to the vibration of the OH group on its surface due to the adsorbed water molecules. Besides, another intense peak was observed at 551.8 cm^{-1} on the surface of $ZnFe_2O_4$. This is due to the vibrational stretching of Fe-O due to the bond created between the tetrahedral Fe ion and the oxygen ion [51]. Interestingly, it was observed that the composites possessed peaks for both photocatalysts, however at intensities proportional to the concentration. This could be evidence of the successful incorporation of $ZnFe_2O_4$ in the g-C_3N_4 heterostructures. Similarly, the dye-sensitized composite displayed highly diminished peaks as compared to the other composites. This confirms that the Eosin Y structure physically bonded well with the composite.

3.1.2. Morphology and Chemical Composition

(1) SEM. From SEM images in Figures 4(a) and 4(b), g-C_3N_4 showed mesoporous nanosheet layers, which was evidence of successful exfoliation, unlike pristine g-C_3N_4 which has been reported to form a bulky and multilayer structure [49].

Similarly, Figures 4(c) and 4(d) show the $ZnFe_2O_4$ images at different magnifications (×100 nm and ×2000 nm). It can be observed that $ZnFe_2O_4$ particles consisted of almost spherical nodules with a diameter ranging between 30.71 nm and 50.97 nm. These particles are highly agglomerated and interlock to form clusters, which could be attributed to the magnetic character of spinel ferrites [47, 51].

Figures 4(e) and 4(f) show the 25% ZF-GCN images at different magnifications (×100 nm and ×1000 nm). It could

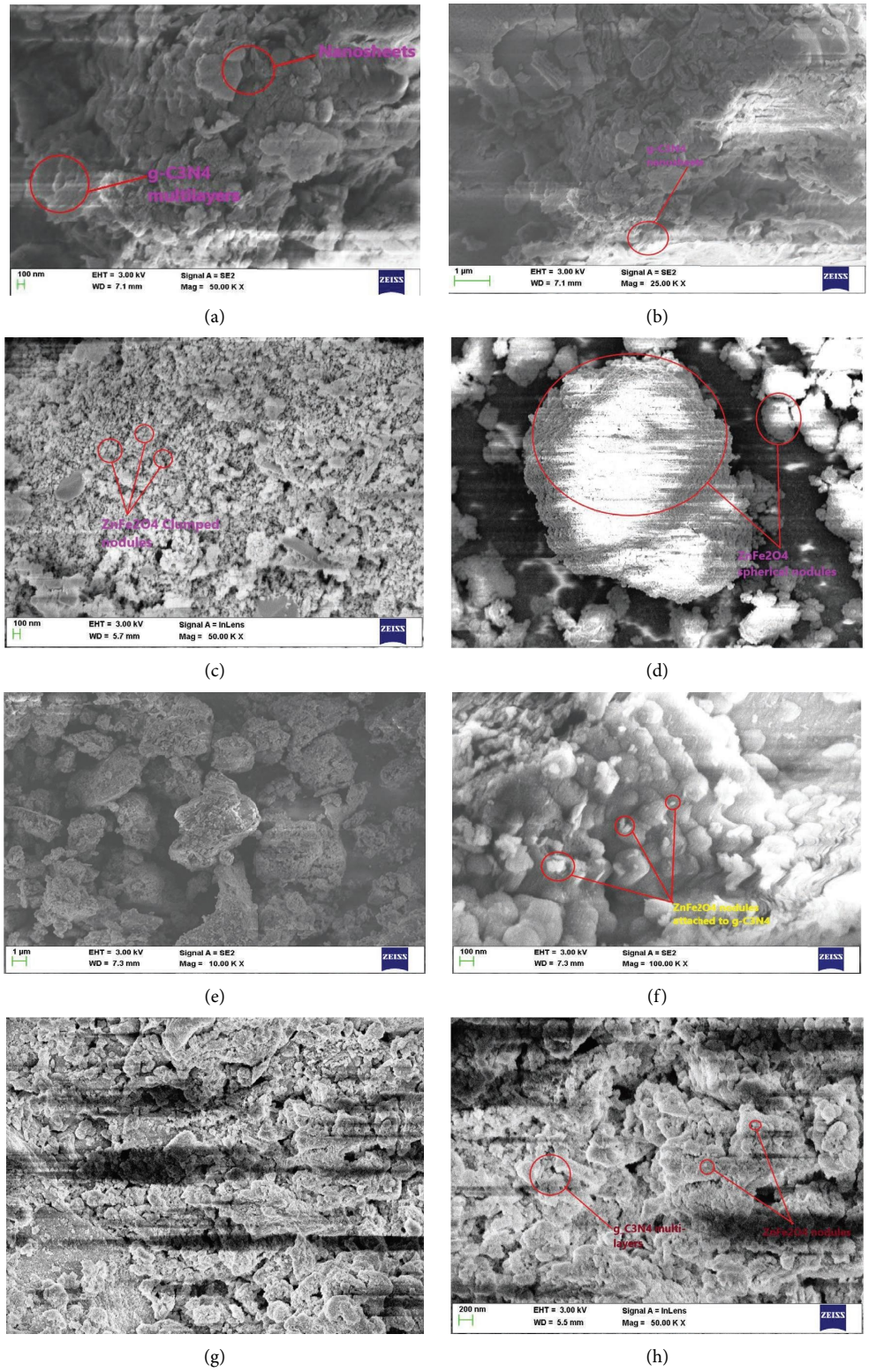

Figure 4: SEM images of (a, b) g-C_3N_4. SEM images of (c, d) $ZnFe_2O_4$. SEM images of (e, f) 25%ZF-GCN. (g) Sensitised-25% ZF-GCN. (h) 25% ZF-GCN.

be observed that $ZnFe_2O_4$ nanoparticles were well dispersed and attached to the sheet-like layers of g-C_3N_4 [46]. Hence, the incorporation of the ferrite nanoparticles into the nanosheets confirmed the successful creation of the heterojunction between the two photocatalysts.

Finally, there were no significant differences in the morphology between the dye-sensitized and 25% ZF-GCN composite in Figures 4(g) and 4(h). This indicates that Eosin Y could not be detected on the surface of the composite using SEM. Furthermore, a similar study conducted by Chen and coworkers using g-C_3N_4 sensitized by indoline dye reported that the TEM images could not detect organic dyes on the surface of a sample [42].

(2) EDX Spectra. The elemental purity of the synthesized photocatalyst was confirmed using energy dispersive X-ray spectroscopy (EDX). Figure 5(a) shows the EDX graph of g-C_3N_4, and this confirmed its purity since carbon, nitrogen, and oxygen peaks were dominant throughout.

Figures 5(b)–5(d) show the EDX spectra for the composites (5%, 25%, and EY-25% $ZnFe_2O_4$/g-C_3N_4). This revealed that peaks of carbon, nitrogen, oxygen, iron, and zinc were detected in all the composites. This confirmed the successful formation of the heterostructures, which supported the SEM, XRD, and FTIR analyses.

3.1.3. Optoelectronic Studies

(1) UV-Vis Absorption Spectra. A UV-Vis spectrophotometer was used to determine the optical absorption of the photocatalyst samples. From Figure 6, it was evident that the synthesized composites had enhanced light absorption in the 400–610 nm region as compared to either of the pure photocatalysts.

The thermally exfoliated graphite carbon nitride nanosheets had a tail absorption of 465 nm, and this agreed with reported literature values [45]. Interestingly, with increasing concentration of zinc ferrite in the composites, there was a gradual red shift in visible light absorption towards higher wavelength. For instance, 5% ZF-GCN, 15% ZF-GCN, and 25% ZF-GCN had corresponding tail absorption of 490 nm, 552 nm, and 610 nm. This corresponded to approximate band gaps of 2.53 eV, 2.23 eV, and 2.03 eV, respectively, when calculated using equation (2). This decrease in the band gap could be possibly explained by the synergy achieved by creating a heterojunction between two semiconductors, which results in band gap modulation and thus broadening of the absorption peak.

Similarly, it can also be observed by increasing the ratio of zinc ferrite in the composite, and there is narrowing in the band gap, which consequently improves the visible light absorption [52]. Furthermore, there was a corresponding colour change of the composite from the light yellow colour characteristic of graphite carbon nitride to brown as the ferrite content is increased. However, the dye-sensitized composite displayed a similar peak to the 25% ZF-GCN. This could be explained by the maximum absorbance of Eosin Y at 550 nm, whose wavelength is lower than that of the composite; hence, it does not extend the visible range.

(2) Photoluminescence Spectra. Apart from extending the visible light absorption spectrum of a photocatalyst, the performance of semiconductors can also be improved further by enhancing charge separation using a heterojunction as well as by inhibiting the recombination rates of electrons/holes pairs. Therefore, to understand the behavior of photoexcited charge mobility, recombination, and transfer for the synthesized photocatalysts, photoluminescence studies were carried out. The photoluminescence (PL) measurements produce an emission peak whose intensity is directly proportional to radiative recombination of photogenerated charges [29]. Hence, a stronger PL emission intensity indicates a higher probability for charge recombination, while a weaker intensity indicates suppressed charge recombination [49]. Figures 7(a) and 7(b) show the PL spectra for g-C_3N_4, $ZnFe_2O_4$ and their corresponding composites excited at 266 nm and 550 nm wavelengths.

It can be observed that graphite carbon nitride has the highest PL spectra intensity, which peaks at approximately 435 nm and coincides with its band gap energy of 2.85 eV. This sharp peak can be attributed to photoexcitation by PL, which caused the $n \longrightarrow \pi^*$ electron transition for lone nitrogen pairs in g-C_3N_4 [53]. Additionally, this phenomenon could be explained by possible radiative recombination of self-trapped charges on the surface of pristine g-C_3N_4 [50].

Interestingly, when the $ZnFe_2O_4$ content was increased in the composites, the intensity of the emission spectrum reduced significantly and could be ranked in the following order: g-C_3N_4 > 5% ZF-GCN > 25% ZF-GCN > EY-25% ZF-GCN > $ZnFe_2O_4$. This is evidence that the synthesized composites can successfully inhibit the charge recombination as well as capture the photoinduced charges, leading to improved separation as compared to g-C_3N_4. Additionally, the heterojunction created between the two pure semiconductors resulted in new electron paths used for evacuating electrons and thus reduced the direct recombination of the photoexcited charges [25]. Besides, there was a notable peak shift of the composite to a higher wavelength, which revealed the possible band-gap reduction after the creation of the heterostructure.

Finally, the dye-sensitized composite (EY-25% ZF-GCN) demonstrated lower PL spectra intensity compared to the 25% ZF-GCN hybrid. This showed the notable improvement in the suppression of charge recombination by dye sensitization and could also explain its slightly higher photocatalytic performance than the latter.

4. Photocatalytic Studies

Immediately after the characterization tests were concluded, all the as-prepared photocatalysts were tested for their degradation and mineralization efficiency at the optimal conditions of 10 mg/l tetracycline, pH 7, 0.7 g/L catalyst, and 90 minutes irradiation time. Figure 8(a) shows the photocatalytic performance of the photocatalysts under solar irradiation.

For the first 15 minutes carried out under dark conditions, the 5, 15, and 25% ZF-GCN composite had a remarkable adsorption efficiency compared to g-C_3N_4 and the

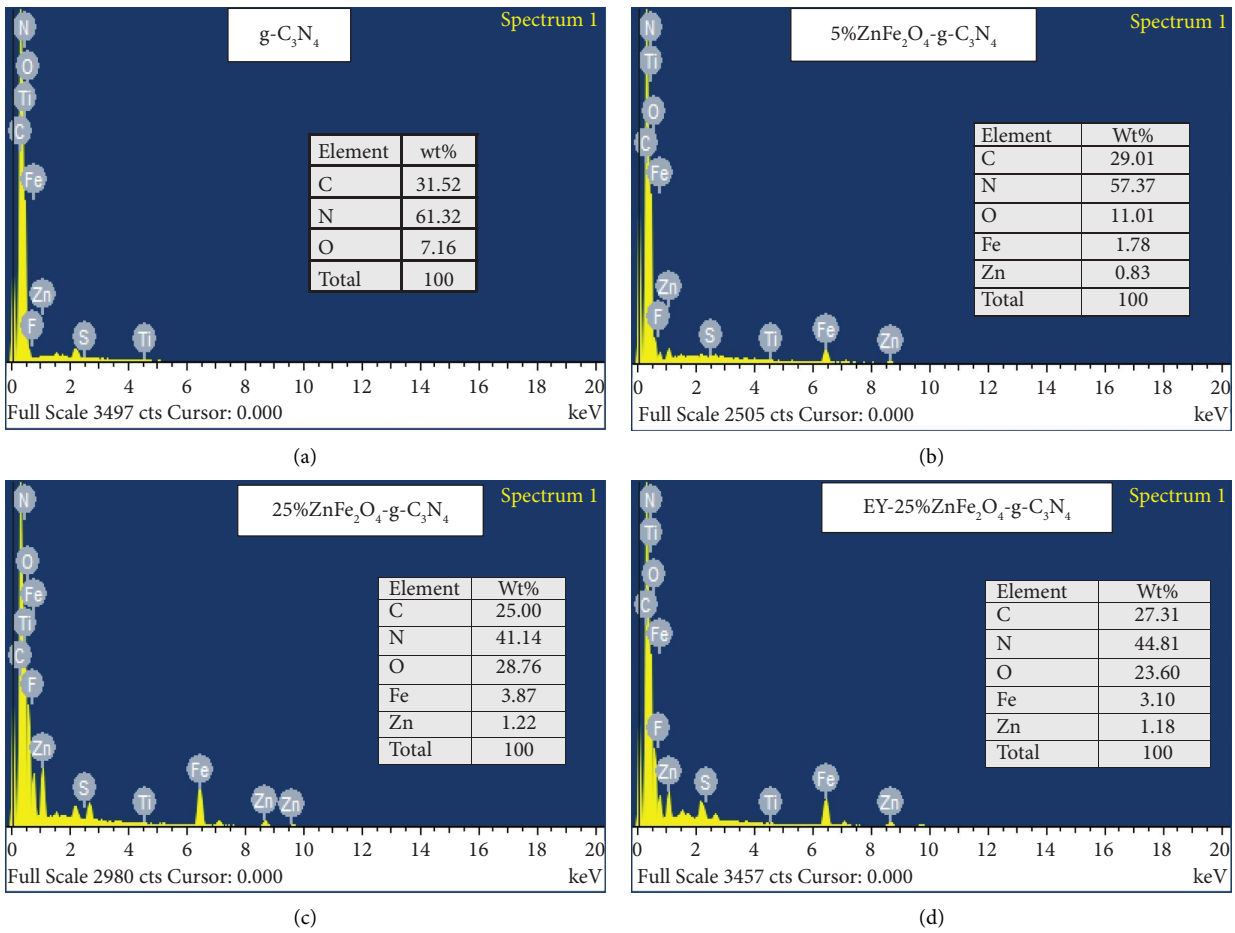

Figure 5: EDX images of (a) g-C_3N_4, (b) 5% $ZnFe_2O_4$/g-C_3N_4, (c) 25% $ZnFe_2O_4$/g-C_3N_4, and (d) EY-25% $ZnFe_2O_4$/g-C_3N_4.

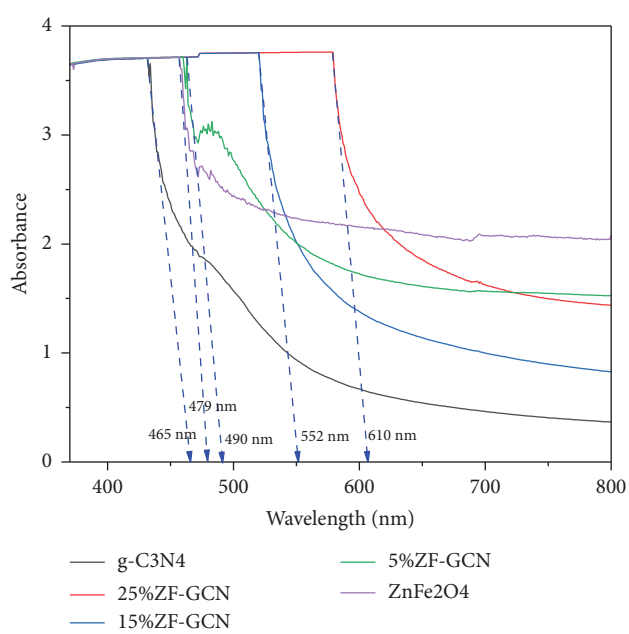

Figure 6: UV-Vis spectra of graphite carbon nitride and zinc ferrite carbon nitride composite (5%, 15%, and 25%).

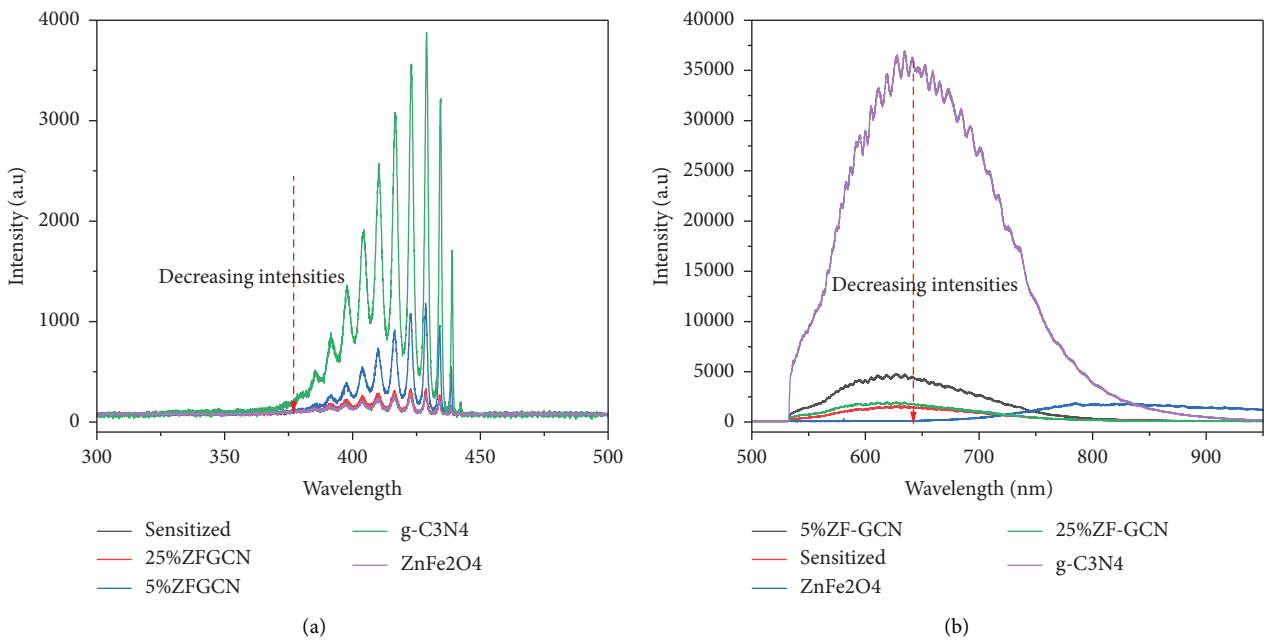

Figure 7: Photoluminescence spectra for samples: (a) 266 nm and (b) 550 nm excitation.

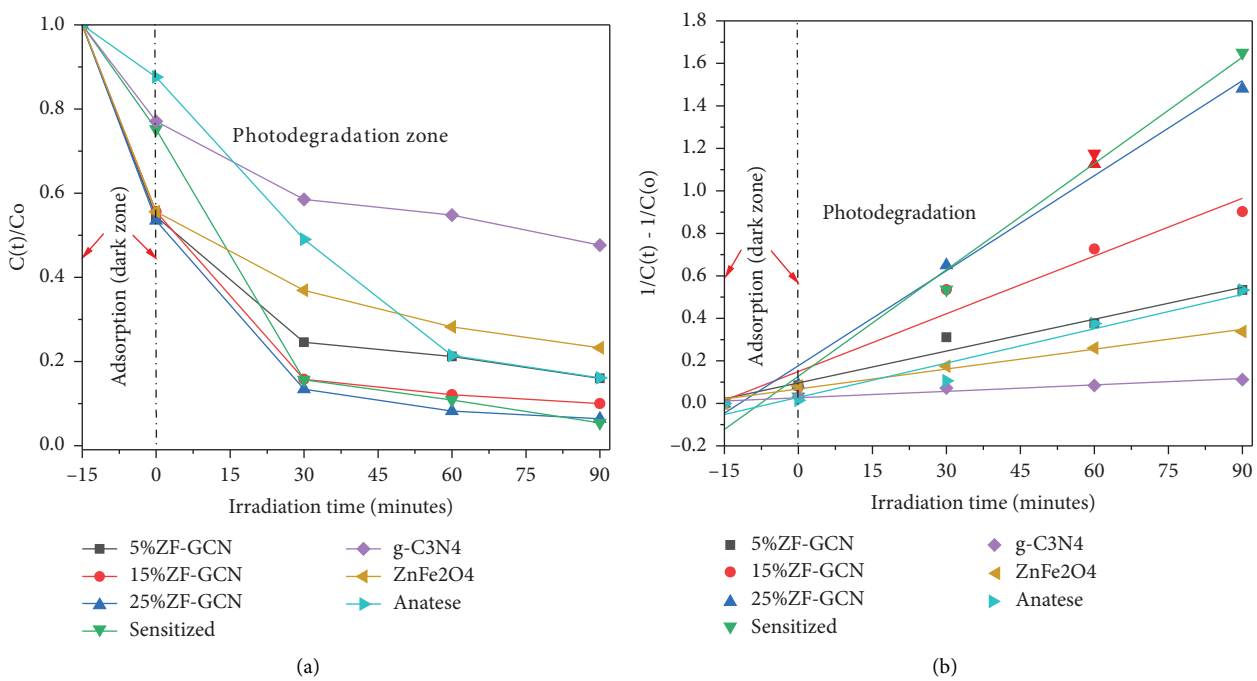

Figure 8: (a) Photodegradation of tetracycline using photocatalysts; (b) tetracycline removal kinetics of photocatalysts.

sensitized composite. The adsorption efficiencies were 12.43%, 22.93%, 24.8%, 44.5%, 44.5%, 45.6%, and 46.6% for anatase, GCN, EY-25% ZF-GCN, ZF, 15% ZF-GCN, 5% ZF-GCN, and 25% ZF-GCN. This can be possibly attributed to the improved surface area and affinity for tetracycline molecules in the composites [54]. However, EY-25% ZF-GCN had a lower adsorption efficiency as compared to other composites. This could be attributed to the possible occupation of its active sites by the dye molecules, hence lowering its adsorptive capacity. Figure 8(a) shows that the degradation efficiency of tetracycline follows the order: EY-25% ZF-GCN > 25% ZF-GCN > 15% ZF-GCN > 5% ZF-GCN > Anatase > ZF > GCN. The sensitized photocatalyst achieves the best photocatalytic performance at 94.62%. This could be explained by the improved charge separation and better light photon harvesting [42]. Similarly, all the composites had significantly higher performance than all the pure photocatalysts, and an increase in $ZnFe_2O_4$

Table 2: Kinetic constant comparison of composites.

Photocatalyst	$k_{app}(\times 10^{-3})$ ($mg^{-1}\cdot L\cdot min^{-1}$)	Comparison with sensitized
Sensitized	16.68	1
25% ZF-GCN	14.91	1.118
15% ZF-GCN	9.16	1.82
Anatase (TiO_2)	5.38	3.10
5% ZF-GCN	5.04	3.31
g-C_3N_4	1.01	16.52
$ZnFe_2O_4$	3.12	5.34

composition was accompanied by an increase in photocatalytic activity. This could be possibly explained by the synergistic interaction between the two semiconductors, which results in prolonged charge separation, higher specific surface area, and enhanced light absorption [46]. However, Chen et al. reported that when the proportion of $ZnFe_2O_4$ is increased above 67% in the composite, there is a significant reduction in photocatalytic activity due to poor dispersion and large crystallite size, which hinder charge mobility [45].

Eventually, the dye-sensitized composite had the best overall photocatalytic performance, as shown by its kinetic rates in Figure 8(b). It outperformed the 25% ZF-GCN 1.118 times, 15% ZF-GCN 1.82 times, 5% ZF-GCN 3.31 times, Anatase-Titania 5.04 times, $ZnFe_2O_4$ 5.34 times, and 16 times better than g-C_3N_4 based on the calculated kinetic rates as shown in Table 2.

The second-order kinetics could fit the degradation data adequately for all the photocatalysts since the coefficient of determination (R^2) ranged between 0.94 and 0.99. See Table S1 in the supplementary material. Therefore, this remarkable improvement in photocatalytic activity is evidence of the potential of dye sensitization as a photocatalyst modification strategy. A similar study by Musa et al. on caffeine degradation using Eosin Y dye-sensitized Ag-TiO_2 and plain Ag-TiO_2 found a higher removal of 95% against 52% in 290 minutes, respectively [28]. Furthermore, a study by Li et al. on the degradation of 2,4-DCP using 15 wt% Eosin Y/$BiPO_4$ composite obtained apparent reaction rates 10.5 fold higher than plain $BiPO_4$ [30]. According to these studies, it can be inferred that Eosin Y sensitization of a photocatalyst improves its photocatalytic performance. However, despite the high photocatalytic activity of the dye-sensitized composite, it was observed that the dye was simultaneously degraded with the pollutant. This agreed with a similar study by Diaz-Angulo et al. who investigated the degradation of diclofenac using methyl red sensitized TiO_2 in a compound parabolic collector [27]. The results revealed better photocatalytic performance with sensitization but simultaneous degradation of the organic dye sensitizer with the pollutant.

A decrease in maximum absorbance intensity for tetracycline as measured by UV/Vis is not evidence for its complete mineralization to CO_2 and H_2O [40]. Furthermore, a decrease in absorbance could be attributed to the destruction of chromophore groups of tetracycline, while TOC reduction depends on mineralization [55]. Therefore, TOC removal was measured for all the composites and pure photocatalysts to determine the extent of mineralization. The TOC removal results showed similar trends to the degradation results obtained by UV/Vis as shown in Figures 9(a) and 9(b).

The TOC removal followed the order: EY-25% ZF-GCN > Anatase > 25% ZF-GCN > 15% ZF-GCN > 5% ZF-GCN > ZF > GCN. The dye-sensitized photocatalyst had the highest removal efficiency of 68.29%, followed closely by anatase (TiO_2) at 64.22%, which proves the comparability of the as-synthesized photocatalyst with that of commercial ones. Interestingly, all the other composites achieved a mineralization efficiency still higher than for the pure photocatalysts. The higher performance of composites compared to pure photocatalysts is evidence of the enhanced photocatalytic activity due to constructing the type-II heterojunction. Furthermore, dye sensitization of the catalyst improves both the degradation and mineralization of pollutants, which can be attributed to the increased generation of oxidative radicals during electron transfer from the excited dye molecule to the conduction band of the photocatalyst [27]. Nonetheless, none of the photocatalysts achieved 100% mineralization of tetracycline, but by increasing the reaction time for photocatalytic systems, it is possible to mineralize all the transformational products [56].

4.1. Comparative Reusability Studies. For heterogenous photocatalysis to be a feasible wastewater treatment method, the as-synthesized photocatalysts should be stable and reusable even after several cycles. Some studies have revealed the recyclability and chemical stability of $ZnFe_2O_4$/g-C_3N_4-based photocatalysts. Dhiman et al. synthesized a g-C_3N_4/$Co_{0.75}Zn_{0.25}Fe_2O_4$ composite, which achieved a degradation efficiency of 92% after five successive cycles against methylene blue. Besides, SEM images of the catalyst collected after the 5th run showed no notable difference with the fresh catalyst. Moreover, leaching tests performed on Co, Fe, and Zn revealed negligible leaching values for consecutive cycles [57]. Similarly, S-g-C_3N_4/$ZnFe_2O_4$ composite maintained a photocatalytic performance of 93% against methylene blue, even after five successful cycles [58]. Therefore, the reported high degradation efficiency, even after cyclic use, indicates that $ZnFe_2O_4$/g-C_3N_4-based composites have high stability and could be viable photocatalysts. Consequently, the next phase of our research will include the recyclability and metal leaching studies.

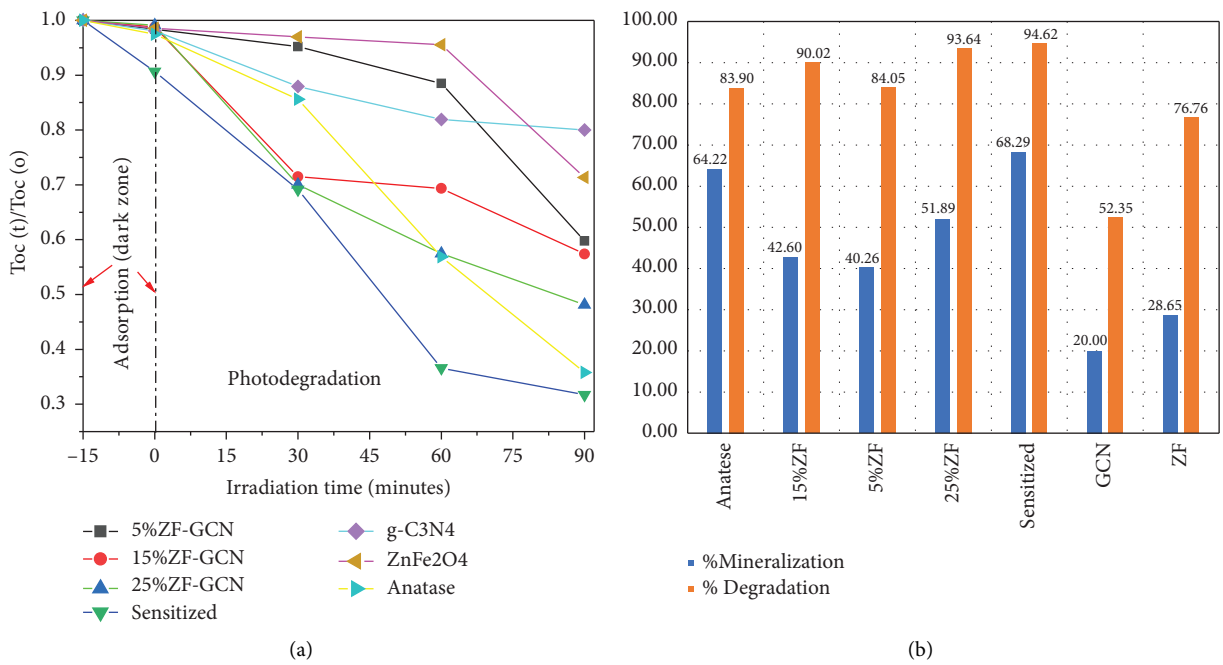

Figure 9: (a) TOC removal of tetracycline; (b) comparison plot for degradation and TOC removal.

5. Conclusions

In this study, Eosin Y-sensitized and plain composites of $ZnFe_2O_4$-g-C_3N_4 were synthesized, characterized, and their photocatalytic performance evaluated by the degradation of tetracycline in aqueous solution. It could be concluded that the construction of a type-II heterojunction between g-C_3N_4 and $ZnFe_2O_4$ is a promising way of improving the photocatalytic performance of both photocatalysts. UV-Vis spectra showed that the 25% composite has enhanced visible light absorption up to 610 nm. The PL spectra also identified a significant decrease in intensity, which is evidence for better charge separation and reduced recombination. All the FTIR, XRD, and SEM-EDX analyses confirmed the presence of the phases for the two semiconductors in the composites. This was evidence of the successful synthesis of the composite. Dye sensitization increased the photocatalytic activity for the composite since it had a photocatalytic and TOC removal of 94.62% and 68.29%, respectively, as compared to 25% ZF-GCN removals of 93.64% and 51.89%. Furthermore, the comparison of the kinetic constants for all the kinetics followed the order: EY-25% ZF-GCN > 25% ZF-GCN > 15% ZF-GCN > Anatase-Titania > 5% ZF-GCN > ZF > GCN. Therefore, the dye-sensitized composite could possibly be applied to remove other emerging pollutants due to its fast kinetics. For future studies, it is recommended that recyclability and metal leaching studies be determined for ZF-GCN composites.

Data Availability

The data used to support the findings of this study are available on request from the corresponding author.

Conflicts of Interest

The authors declare that there are no conflicts of interest regarding the publication of this paper.

Acknowledgments

The authors are grateful for the financial support obtained from Kenya's National Research Fund (Grant no. 2/MMC/825) by funding this project under the Sustainable Technologies for Potable Water Treatment programme.

Supplementary Materials

The equipment setup of the photocatalytic experiment and the second-order fitting data are described here. (*Supplementary Materials*)

References

[1] A. R. L. Ribeiro, D. Hermosilla, M. A. Mueses, R. Xiao, D. Mantzavinos, and D. Mantzavinos, "Advanced oxidation technologies for water/wastewater treatment: advances, gaps and challenges- Editorial," *Chemical Engineering Journal Advances*, vol. 10, Article ID 100272, 2022.

[2] C. Thambiliyagodage, "Efficient photocatalysis of carbon coupled TiO2 to degrade pollutants in wastewater – a review," *Environmental Nanotechnology, Monitoring & Management*, vol. 18, Article ID 100737, 2022.

[3] K. O. K'oreje, M. Okoth, H. Van Langenhove, and K. Demeestere, "Occurrence and treatment of contaminants of emerging concern in the African aquatic environment: literature review and a look ahead," *Journal of Environmental Management*, vol. 254, Article ID 109752, 2020.

[4] L. C. Mahlalela, C. Casado, J. Marugán, S. Septien, T. Ndlovu, and L. N. Dlamini, "Coupling biological and photocatalytic

treatment of atrazine and tebuthiuron in aqueous solution," *Journal of Water Process Engineering*, vol. 40, Article ID 101918, 2021.

[5] C. Guo, M. Cheng, G. Zhang et al., "Degradation of organic contaminants by peroxymonosulfate activated with zeolitic imidazolate framework-based catalysts: performances, mechanisms and stability," *Environmental Science: Nano*, vol. 10, no. 6, pp. 1528–1552, 2023.

[6] D. C. Khandekar and R. Bandyopadhyaya, "Design of a TiO 2 coated film in a batch reactor: nanoparticle film synthesis and optimization for contaminant degradation and modeling," *Industrial and Engineering Chemistry Research*, vol. 60, no. 48, pp. 17509–17519, 2021.

[7] N. Liu, Z. Sun, H. Zhang, L. H. Klausen, R. Moonhee, and S. Kang, "Emerging high-ammonia-nitrogen wastewater remediation by biological treatment and photocatalysis techniques," *Science of the Total Environment*, vol. 875, Article ID 162603, 2023.

[8] A. Balakrishnan, M. Chinthala, R. K. Polagani, and D. V. N. Vo, "Removal of tetracycline from wastewater using g-C 3 N 4 based photocatalysts: a review," *Environmental Research*, vol. 216, no. P3, Article ID 114660, 2023.

[9] Y. Deng, L. Tang, G. Zeng et al., "Facile fabrication of mediator-free Z-scheme photocatalyst of phosphorous-doped ultrathin graphitic carbon nitride nanosheets and bismuth vanadate composites with enhanced tetracycline degradation under visible light," *Journal of Colloid and Interface Science*, vol. 509, pp. 219–234, 2018.

[10] M. Li, M. Chen, S. L. J. Lee, S. Lin, and S. Lin, "Facile fabrication of a 2D/2D CoFe- LDH/g- C 3 N 4 nanocomposite with enhanced photocatalytic tetracycline degradation," *Environmental Science and Pollution Research*, vol. 30, no. 2, pp. 4709–4720, 2022.

[11] J. Shan, X. Wu, C. Li et al., "Photocatalytic degradation of tetracycline hydrochloride by a Fe3O4/g-C3N4/rGO magnetic nanocomposite mechanism: modeling and optimization," *Environmental Science and Pollution Research*, vol. 30, no. 3, pp. 8098–8109, 2023.

[12] M. Jia, Q. Liu, W. Xiong et al., "Ti3+ self-doped TiO2 nanotubes photoelectrode decorated with Ar-Fe2O3 derived from MIL-100(Fe): enhanced photo-electrocatalytic performance for antibiotic degradation," *Applied Catalysis B: Environmental*, vol. 310, Article ID 121344, 2022.

[13] H. Peng, W. Xiong, Z. Yang et al., "Fe3O4-supported N-doped carbon channels in wood carbon form etching and carbonization: boosting performance for persulfate activating," *Chemical Engineering Journal*, vol. 457, pp. 141317–141411, 2023.

[14] P. Wang, C. Xu, X. Zhang, Q. Yuan, and S. Shan, "Effect of photocatalysis on the physicochemical properties of liquid digestate," *Environmental Research*, vol. 223, Article ID 115467, 2023.

[15] R. Gusain, N. Kumar, and S. S. Ray, "Factors influencing the photocatalytic activity of photocatalysts in wastewater treatment," *Photocatalysts in Advanced Oxidation Processes for Wastewater Treatment*, pp. 229–270, 2020.

[16] H. M. Shu, J. M. Xie, H. Xu, H. M. Li, Y. G. Xu, and Z. Gu, "Characterization and photocatalytic activity of ZnO/AgNbO3," *Journal of Inorganic Materials*, vol. 25, no. 9, pp. 935–941, 2010.

[17] N. Rono, J. K. Kibet, B. S. Martincigh, and V. O. Nyamori, "A review of the current status of graphitic carbon nitride," *Critical Reviews in Solid State and Materials Sciences*, vol. 46, no. 3, pp. 189–217, 2020.

[18] S. B. Patel, A. Tripathi, and A. P. Vyas, "Recent development in the structural modification of graphitic carbon nitride for sustainable photocatalysis: advances, challenges and opportunities," *Environmental Nanotechnology, Monitoring and Management*, vol. 16, Article ID 100589, 2021.

[19] Y. Wang, H. Song, J. Chen et al., "A novel solar photo-Fenton system with self-synthesizing H 2 O 2: enhanced photo-induced catalytic performances and mechanism insights," *Applied Surface Science*, vol. 512, Article ID 145650, 2020.

[20] H. V. Duc, N. T. A. Thu, D. T. N. Cam et al., "Synthesis, characterization, and photocatalytic activity of multicomponent CdMoO4/g-C3N4/GO composite," *Environmental Engineering Research*, vol. 28, no. 6, pp. 220649-220650, 2023.

[21] V. Raja and B. Jaffar Ali, "Colloids and Surfaces A: physicochemical and Engineering Aspects Synergy of photon upconversion and Z-scheme mechanism in graphitic carbon nitride nanoparticles decorated g-C 3 N 4-TiO 2," *Colloids and Surfaces A: Physicochemical and Engineering Aspects*, vol. 611, Article ID 125862, 2021.

[22] K. K. Das, S. Patnaik, S. Mansingh et al., "Enhanced photocatalytic activities of polypyrrole sensitized zinc ferrite/graphitic carbon nitride n-n heterojunction towards ciprofloxacin degradation, hydrogen evolution and antibacterial studies," *Journal of Colloid and Interface Science*, vol. 561, pp. 551–567, 2020.

[23] S. R. Chowdhury, F. Alhelal, M. Alahmadi, and N. Alqahtani, "An overview on major design constraints, impact and challenges for a conventional wastewater treatment design," *Journal of Environmental Treatment Techniques*, vol. 9, no. 1, pp. 7–16, 2020.

[24] S. Borthakur and L. Saikia, "ZnFe 2 O 4 @ g-C 3 N 4 nanocomposites: an e ffi cient catalyst for Fenton-like photodegradation of environmentally pollutant Rhodamine B," *Journal of Environmental Chemical Engineering*, vol. 7, Article ID 103035, 2019.

[25] S. Renukadevi and A. P. Jeyakumari, "Rational design of ZnFe 2 O 4/g-C 3 N 4 heterostructures composites for high efficient visible-light photocatalysis for degradation of aqueous organic pollutants," *Inorganic Chemistry Communications*, vol. 118, Article ID 108047, 2020.

[26] K. K. Kefeni and B. B. Mamba, "Photocatalytic application of spinel ferrite nanoparticles and nanocomposites in wastewater treatment: review," *Sustainable Materials and Technologies*, vol. 23, Article ID e00140, 2020.

[27] J. Diaz-angulo, A. Arce-sarria, M. Mueses, A. Hernandez-ramirez, and F. Machuca-martinez, "Analysis of two dye-sensitized methods for improving the sunlight absorption of TiO2 using CPC photoreactor at pilot scale," *Materials Science in Semiconductor Processing*, vol. 103, Article ID 104640, 2019.

[28] M. M. Ibrahim and U. I. Gaya, "Synthesis of eosin Y-sensitized Ag-TiO2 nano-hybrid for optimized photocatalytic degradation of aqueous caffeine," *Journal of the Chilean Chemical Society*, vol. 64, no. 1, pp. 4275–4284, 2019.

[29] H. You, "Synthesis, characterization and visible photocatalytic performance of iron (III) tetracarboxyphthalocyanine-sensitized TiO2 photocatalyst," *Journal of Physical Chemistry and Biophysics*, vol. 6, no. 1, pp. 2–6, 2016.

[30] B. Li, Y. Zhang, F. Duanmu, Y. Shen, Z. Shen, and S. Zhong, "Eosin Y sensitized BiPO 4 nanorods for bi-functionally enhanced visible-light-driven photocatalysis," *Photochemical and Photobiological Sciences*, vol. 18, no. 6, pp. 1408–1418, 2019.

[31] F. D. J. Silerio-Vázquez, C. M. Núñez-Núñez, M. T. Alarcón-Herrera, and J. B. Proal-Nájera, "Comparative efficiencies for

phenol degradation on solar heterogeneous photocatalytic reactors: flat plate and compound parabolic collector," *Catalysts*, vol. 12, pp. 575-576, 2022.

[32] M. A. Fendrich, A. Quaranta, M. Orlandi, M. Bettonte, and A. Miotello, "Solar concentration for wastewaters remediation: a review of materials and technologies," *Applied Sciences*, vol. 9, no. 1, p. 118, 2018.

[33] G. Pucar Milidrag, J. Nikić, V. Gvoić et al., "Photocatalytic degradation of magenta effluent using magnetite doped TiO2 in solar Parabolic Trough concentrator," *Catalysts*, vol. 12, no. 9, pp. 986–1020, 2022.

[34] Y. Abdel-Maksoud, E. Imam, and A. Ramadan, "TiO2 solar photocatalytic reactor systems: selection of reactor design for scale-up and commercialization—analytical review," *Catalysts*, vol. 6, pp. 138-139, 2016.

[35] R. Binjhade, R. Mondal, and S. Mondal, "Continuous photocatalytic reactor: critical review on the design and performance," *Journal of Environmental Chemical Engineering*, vol. 10, no. 3, Article ID 107746, 2022.

[36] D. Wang, M. A. Mueses, J. A. C. Márquez et al., "Engineering and modeling perspectives on photocatalytic reactors for water treatment," *Water Research*, vol. 202, Article ID 117421, 2021.

[37] M. Ghaedi, V. Madadi, Z. Moradi, V. A. L. Roy, and H. Heidari, "Chemical Engineering Research and Design S-scheme heterojunction g-C 3 N 4/TiO 2 with enhanced photocatalytic activity for degradation of a binary mixture of cationic dyes using solar Mohammad Hossein Barzegar a, Mohammad Mehdi Sabzehmeidani b," *Chemical Engineering Research and Design*, vol. 174, pp. 307–318, 2021.

[38] S. Rani, A. Garg, and N. Singh, "Efficient degradation of doxycycline and ofloxacin in an aqueous environment using Fe and Cu doped TiO2-SiO2 photocatalyst under sunlight," *Environmental Engineering Research*, vol. 27, no. 4, pp. 210282–210290, 2021.

[39] S. Xu, H. Zhu, W. Cao et al., "Cu-Al2O3-g-C3N4 and Cu-Al2O3-C-dots with dual-reaction centres for simultaneous enhancement of Fenton-like catalytic activity and selective H2O2 conversion to hydroxyl radicals," *Applied Catalysis B: Environmental*, vol. 234, no. April, pp. 223–233, 2018.

[40] W. Jo, S. Moru, and S. Tonda, "Magnetically responsive SnFe2O4/g-C3N4 hybrid photocatalysts with remarkable visible-light-induced performance for degradation of environmentally hazardous substances and sustainable hydrogen production," *Applied Surface Science*, vol. 506, Article ID 144939, 2020.

[41] X. Rong, S. Liu, M. Xie et al., "N 2 photo fi xation by Z-scheme single-layer g-C 3 N 4/ZnFe 2 O 4 for cleaner ammonia production," *Materials Research Bulletin*, vol. 127, Article ID 110853, 2020.

[42] Y. Chen, Y. Liu, and Z. Ma, "G-c3 n4 sensitized by an indoline dye for photocatalytic h2 evolution," *Processes*, vol. 9, no. 6, pp. 1055–1115, 2021.

[43] M. Tigabu Bekele, "Synthesis and characterization of CdS/CeO2 Nanocomposite with improved visible-light photocatalytic degradation of methyl orange dye," *Journal of Plant Science and Phytopathology*, vol. 6, no. 2, pp. 065–074, 2022.

[44] A. C. Mecha, M. S. Onyango, A. Ochieng, T. S. Jamil, C. J. S. Fourie, and M. N. B. Momba, "UV and solar light photocatalytic removal of organic contaminants in municipal wastewater," *Separation Science and Technology*, vol. 51, no. 10, pp. 1765–1778, 2016.

[45] L. Chen, W. Ma, J. Dai, J. Zhao, C. Li, and Y. Yan, "Journal of Photochemistry and Photobiology A: chemistry heterostructures enhanced visible-light photocatalysis for spiramycin degradation," *Journal of Photochemistry and Photobiology A: Chemistry*, vol. 328, pp. 24–32, 2016.

[46] A. S. Basaleh, "Construction of mesoporous ZnFe2O4-g-C3N4nanocomposites for enhanced photocatalytic degradation of acridine orange dye under visible light illumination adopting soft- and hard-template-assisted routines," *Journal of Materials Research and Technology*, vol. 11, pp. 1260–1271, 2021.

[47] H. Saeed, N. Nadeem, M. Zahid et al., "Mixed metal ferrite(Mn 0. 6 Zn 0. 4 Fe 2 O 4) intercalated g-C 3 N 4 nanocomposite: ef fi cient sunlight driven photocatalyst for methylene blue degradation," *Nanotechnology*, vol. 32, no. 50, Article ID 505714, 2021.

[48] B. Palanivel, V. Jayaraman, C. Ayyappan, and M. Alagiri, "Magnetic binary metal oxide intercalated g-C 3 N 4: energy band tuned p-n heterojunction towards Z-scheme photo-Fenton phenol reduction and mixed dye degradation," *Journal of Water Process Engineering*, vol. 32, Article ID 100968, 2019.

[49] Q. Huang, Q. Zhao, C. Yang, and T. Jiang, "Facile synthesis of mesoporous graphitic carbon nitride/SnO 2 nanocomposite photocatalysts for the enhanced photodegradation of Rhodamine B," *Reaction Kinetics, Mechanisms and Catalysis*, vol. 129, no. 1, pp. 535–550, 2020.

[50] B. Gao, J. Wang, M. Dou, C. Xu, and X. Huang, "Enhanced photocatalytic removal of amoxicillin with Ag/TiO2/mesoporous g-C3N4 under visible light: property and mechanistic studies," *Environmental Science and Pollution Research*, vol. 27, no. 7, pp. 7025–7039, 2020.

[51] K. Jangam, K. Patil, S. Balgude, S. Patange, and P. More, "Synthesis and characterization of magnetically separable Zn1-xCoxFeMnO4 nanoferrites as highly efficient photocatalyst for degradation of dye under solar light irradiation," *Journal of Physics and Chemistry of Solids*, vol. 148, Article ID 109700, 2021.

[52] B. Palanivel and A. Mani, "Conversion of a type-II to a Z-scheme heterojunction by intercalation of a 0D electron mediator between the integrative NiFe2O4/g-C3N4Composite nanoparticles: boosting the radical production for photo-fenton degradation," *American Chemical Society Omega*, vol. 5, no. 31, pp. 19747–19759, 2020.

[53] A. O. Oluwole and O. S. Olatunji, "Enhanced photocatalytic degradation of naproxen in aqueous matrices using reduced graphene oxide (rGO) decorated binary BSO/g-C 3 N 4 heterojunction nanocomposites," *Chemical Engineering Journal Advances*, vol. 12, Article ID 100417, 2022.

[54] N. Liu, R. Qi, X. Sun, N. Kawazoe, G. Chen, and Y. Yang, "Synthesis and characterization of 3D-zeolite–modified TiO2-based photocatalyst with synergistic effect for elimination of organic pollutant in wastewater treatment," *Frontiers in Environmental Science*, vol. 10, pp. 1–12, 2022.

[55] G. Pucar, M. Prica, D. Kerkez, and B. Dalmacija, "Journal of the Taiwan Institute of Chemical Engineers A comparative study of the decolorization capacity of the solar-assisted Fenton process using ferrioxalate and Al, Fe-bentonite

catalysts in a parabolic trough reactor," *Journal of Taiwan Institution of Chemical Engineers*, vol. 93, pp. 436–449, 2018.

[56] D. Adenuga, S. Skosana, S. Tichapondwa, and E. Chirwa, "Synthesis of a plasmonic AgCl and oxygen-rich Bi24O31-Cl10composite heterogeneous catalyst for enhanced degradation of tetracycline and 2,4-dichlorophenoxy acetic acid," *Royal Society of Chemistry Advances*, vol. 11, no. 58, pp. 36760–36768, 2021.

[57] P. Dhiman, A. Kumar, G. Rana, and G. Sharma, "g-C3N4 stacked Co0.75Zn0.25Fe2O4 magnetically separable nano hybrids for intensified removal of methylene blue under UV–Visible light," *Inorganic Chemistry Communications*, vol. 153, Article ID 110864, 2023.

[58] S. S. Hassan, M. Javed, M. N. Akhtar et al., "The photocatalytic and antibacterial potential of highly efficient S-scheme binary S-gC 3 N 4 @ Co-zinc ferrite nanocomposite," *Optical Materials*, vol. 142, Article ID 114046, 2023.